To be submitted to IEEE Trans. Geosci. & Remote Sens., 1998

Saline Ice Thickness Retrieval under Diurnal Thermal Cycling Conditions

S. E. Shih, K. H. Ding, and J. A. Kong
Department of Electrical Engineering and Computer Science
and Research Laboratory of Electronics
Massachusetts Institute of Technology
Cambridge, MA 02139

S. V. Nghiem
Center for Space Microelectronics Technology
Jet Propulsion Laboratory
California Institute of Technology
Pasadena, CA 91109

A. K. Jordan
Remote Sensing Division
Naval Research Laboratory
Washington, DC 20375

Mailing address : Dr. S. V. Nghiem, Jet Propulsion Laboratory
Mail Stop 300-235, 4800 Oak Grove Drive, Pasadena, CA 91109

Saline Ice Thickness Retrieval under Diurnal Thermal Cycling Conditions

Shih-En Shih, Kung-Hau Ding, and Jin Au Kong
Department of Electrical Engineering and Computer Science
and Research Laboratory of Electronics
Massachusetts Institute of Technology, Cambridge, MA 02139

Son V. Nghiem
Center for Space Microelectronics Technology
Jet Propulsion Laboratory
California Institute of Technology, Pasadena, CA 91109

Arthur K. Jordan
Remote Sensing Division
Naval Research Laboratory, Washington, DC 20375

Abstract

An inversion algorithm is presented to reconstruct ice growth under thermal cycling conditions by using time-series active microwave measurements. The method uses a direct scattering model consisting of a one-dimensional thermodynamic model of saline ice growth that includes the thermal interactions with atmosphere, and a physical-based electromagnetic model that takes into account the thermal and electromagnetic properties of ice and the combined volume and surface scattering effects. The combined thermodynamic electromagnetic scattering model is applied to interpret the CRRELEX 94 experimental observations on both the ice growth and the diurnal cycles in the C-band polarimetric backscatter. The crucial part of the inversion algorithm is to use sequentially measured radar data together with the developed direct scattering model to retrieve the sea ice parameters. The algorithm is applied to the CRRELEX 94 data and successfully reconstruct the evolution of ice growth under a thermal cycling environment. This work shows that the inversion algorithm using time-series data offers a distinct accuracy over the algorithms using only individual microwave data.

I. INTRODUCTION

Sea ice thickness is an important parameter in the heat exchange between the ocean and the atmosphere and mass balance of polar oceans [1]. Satellite remote sensing offers ample opportunities to monitor sea ice routinely. Thus, to retrieve ice thickness using remote sensing data becomes an attractive and important issue for the sea ice research community. In the past two decades, there have been considerable studies regarding the microwave signatures of sea ice [2–4], and both passive and active spaceborne sensor images have been applied in mapping the ice extent and identifying the ice types [5,6]. However, there still remains a basic issue for a direct determination of sea ice thickness from space. Some recent work has addressed on using electromagnetic remote sensing data to retrieve sea ice thickness [6–8].

In a previous paper [8], we have developed an ice thickness retrieval algorithm that uses time-series active microwave data and an electromagnetic scattering model consisting of an ice constant growth model. This inversion algorithm was applied and accurately reconstructed the thickness of a laboratory-grown thin saline ice sheet by using the C-band polarimetric radar measurements from CRRELEX 93 experiment [9]. It was found that by incorporating the ice growth model into the inversion algorithm, the thickness estimation can be constrained sufficiently to predict more accurate results. In addition, the use of time series data is helpful for resolving the non-uniqueness and stability problems which are common for parametric estimation methods.

The formation and growth of sea ice is generally influenced by the changing environmental conditions. The thermal interaction between sea ice and atmosphere strongly affects the thermodynamic processes within the ice layer. The thermally varying ice physical properties also significantly alter the electromagnetic interactions with the sea ice medium. In this study, we extend our previous work to investigate the retrieval of ice thickness under a thermal cycling growth condition. A one-dimensional thermodynamic model of sea ice is constructed, that includes the thermal interactions between ice and atmosphere, desalination effect, and brine volume thermal variation, to characterize the saline ice physical properties under thermodynamically varying conditions. An electromagnetic model based on the radiative transfer theory with multilayer structure and rough interface is used to calculate wave propagation and scattering in the ice medium. Small perturbation method is applied to account for the sea ice surface roughness [10]. The combined thermodynamic electromagnetic scattering model is applied to interpret the CRRELEX 94 experimental observations

on both the ice growth and the diurnal cycles in the C-band polarimetric backscatter. As in the previous study, this direct scattering model is then employed in a parametric estimation scheme and uses time-series measured data to construct the inversion algorithm.

The CRRELEX 94 experiment [11], which was carried out at the outdoor Geophysical Research Facility in the U.S. Army Cold Regions Research and Engineering Laboratory (CRREL) during January 19–22, 1994, is briefly described in Section II. In Section III, the saline ice thermodynamic electromagnetic scattering model is developed. This direct scattering model consists of a saline ice physical model describing the dynamic variation of ice characteristics coupled with an electromagnetic scattering model accounting for wave propagation and scattering in a random medium. Interpretations of CRRELEX 94 measurements on the diurnal ice radar signatures are also demonstrated in this section. The inversion algorithm using time series data based on this direct scattering model and a parametric estimation approach is described in Section IV. The ice thickness retrieval and comparisons with CRRELEX 94 ground truth are also presented in this section, followed by summary section.

II. CRRELEX 94 SALINE ICE EXPERIMENT

The varying environmental conditions affect the growth process of ice which in turn influence the interaction between electromagnetic radiation and ice. To investigate the diurnal thermal effects on the polarimetric C-band radar signatures of sea ice, laboratory experiments were carried out at the outdoor Geophysical Research Facility in CRREL during January 1994. A more detailed description about the experimental set up, procedures, and findings can be found in [11].

In the CRRELEX 94, an ice sheet was grown from open saline water with an initial salinity of 30.0 $^0/_{00}$, the growth lasted for three days until the ice grown up to 10 cm in thickness. To characterize the ice physical properties, samples were taken from the pond to measure their thickness, temperature, and salinity for approximately every 1 cm during the ice growth. The evolution of ice thickness is shown in Figure 1(a), where circles represents the measurements and the continuous curve is obtained from an ice growth model which will be described in the next section. The desalination is shown in Figure 1(b), where a roughly 30% brine loss is observed as the thickness reached 10 cm. The linear fitted curve has an extrapolated value of salinity at $h = 0$, S_{i0}, be 12.0 $^0/_{00}$ and a negative slope of 0.458 $^0/_{00}$ per cm. The meteorological information, including air temperature, short-wave (0.3 to 3 μm)

and long-wave (3 to 50 μm) solar radiations, wind speed, relative humidity, and air pressure, were collected by a nearby weather station. The integrated values of short-wave and long-wave radiation are shown in Figure 2(a), and the measured air temperature and ice surface temperature are shown in Figure 2(b). From Figures 1 and 2, it shows that the variation of growth rate is consistent with the change of incident radiation and air temperature. A slowdown in the ice growth during the second day in Figure 1(a) corresponds to the warming daytime in Figure 2(a).

During the course of experiment, time-series of C-band (5 GHz) polarimetric backscatter data were collected at roughly every centimeter of ice growth and at various incidence angles. The measured co-polarization (HH and VV) backscattering coefficients are shown in Figures 3(a) and 3(b) for 30° and 40° incidence angles, respectively. The backscatter signatures show a substantial diurnal variation of 4-6 dB for both polarizations. As shown in the same figure, the backscatter variation is also synchronous and well correlated with the temperature cycle. It suggests that the scattering mechanism is related to the diurnal variations of the thermophysical properties of sea ice. Toward the later stage of experiment, more frost flowers appeared on the ice surface which may increase the rough surface scattering effect, especially at small incidence angles [11].

III. THERMODYNAMIC ELECTROMAGNETIC SCATTERING MODEL

As indicated in the previous section, the temperature variation of ice physical properties is important in the interpretation of sea ice diurnal electromagnetic characteristics. In this section, we present an extension of the sea ice scattering model developed in [8] to further take into account the thermal cycling environmental conditions, the diurnal ice growth, and the rough air-ice interface scattering effect. Applications of this diurnal scattering model are demonstrated by comparing the simulations with the measured ice growth and radar backscatters in this section, and the ice thickness retrieval in Section IV.

A. Electromagnetic Scattering Model

Radiative transfer theory is applied in this study to consider the combined volume and rough surface scattering effects of sea ice medium [10]. A three layer discrete random medium model with rough interface, as shown in Figure 4, is used to represent the scattering configuration. The uppermost medium is air with permittivity ϵ_o and the lower half space

is saline water with complex permittivity ϵ_w. The rough air-ice interface is assumed to be Gaussian with mean surface at $z = 0$, and the roughness is described by the correlation length l and the root mean square (rms) height s. The sea ice layer is divided into two sub-layers of thicknesses h_1 and h_2. The brine inclusions in the lower sea ice layer ($-h_1 - h_2 < z < -h_1$) are assumed to be vertically oriented, but are randomly oriented in the upper sea ice layer ($-h_1 < z < 0$), which corresponds to the incubation layer described in [11]. The background medium of sea ice is pure ice with complex permittivity ϵ_i. The ellipsoids of semi-axes a_n, b_n, and c_n (n=1, 2) represent the brine pockets in the n-th ice layer. The complex permittivities of brine inclusions are ϵ_{bn}, and their fractional volumes are f_{vn}. These model parameters are subject to dynamic changes during the ice growth process.

In each sea ice layer, the wave propagation and scattering can be described by the radiative transfer equations [10],

$$\cos\theta \frac{d\bar{I}_n(\theta,\phi,z)}{dz} = -\bar{\bar{\kappa}}_{en}(\theta,\phi)\cdot\bar{I}_n(\theta,\phi,z) + \int_{4\pi} d\Omega' \bar{\bar{P}}_n(\theta,\phi;\theta',\phi')\cdot\bar{I}_n(\theta',\phi',z) \qquad (1)$$

with n=1, 2, $0 \le \theta \le \pi$, and $0 \le \phi \le 2\pi$. In (1), $\bar{I}_n$ represents the Stokes vector, $\bar{\bar{\kappa}}_{en}$ the extinction matrix which includes both scattering and absorption losses, and $\bar{\bar{P}}_n(\theta,\phi;\theta',\phi')$ the phase matrix which describes how particles scatter radiation from the direction (θ',ϕ') into the direction (θ,ϕ), in the n-th layer. The elements of extinction matrix and phase matrix for small ellipsoids with prescribed orientation distribution are given in [10].

The boundary conditions for the vector radiative transfer equations are as follows. At $z = 0$,

$$\begin{aligned}\bar{I}_1(\pi-\theta,\phi,z=0) &= \int_0^{2\pi} d\phi' \int_0^{\pi/2} d\theta' \sin\theta' \bar{\bar{R}}_{10}(\theta,\phi;\theta',\phi')\cdot\bar{I}_1(\theta',\phi',z=0) \qquad (2)\\ &+ \bar{\bar{T}}_{01}(\theta,\phi;\theta_{0i},\phi_{0i})\cdot\bar{I}_{0i}(\pi-\theta_{0i},\phi_{0i}),\end{aligned}$$

at $z = -h_1$,

$$\bar{I}_1(\theta,\phi,z=-h_1) = \bar{I}_2(\theta,\phi,z=-h_1) \qquad (3)$$

$$\bar{I}_2(\pi-\theta,\phi,z=-h_1) = \bar{I}_1(\pi-\theta,\phi,z=-h_1), \qquad (4)$$

and at $z = -h_1 - h_2$,

$$\bar{I}_2(\theta,\phi,z=-h_1-h_2) = \bar{\bar{R}}_{23}(\theta,\phi)\cdot\bar{I}_2(\pi-\theta,\phi,z=-h_1-h_2) \qquad (5)$$

for $0 \le \theta \le \pi/2$. In (2), $\bar{I}_{0i}(\pi-\theta_{0i},\phi_{0i})$ is the incident Stokes vector in region 0 (air) from direction $(\pi-\theta_{0i},\phi_{0i})$, and $\bar{\bar{T}}_{01}$ and $\bar{\bar{R}}_{10}$ are the respective transmission and reflection

matrices for the rough interface between regions 0 and 1 (upper sea ice layer). In this study, $\overline{\overline{T}}_{01}$ and $\overline{\overline{R}}_{10}$ are calculated based on the small perturbation method (SPM) [10], detailed expressions of these matrices are given in the Appendix. The matrix $\overline{\overline{R}}_{23}$ in (5) is the reflection matrix for the flat interface between regions 2 (lower sea ice layer) and 3 (sea water) [10]. The effects of reflection and refraction between regions 1 and 2 are neglected due to the small difference between their effective permittivities.

The radiative transfer equations (1) together with the boundary conditions (2)-(5) are solved using the discrete eigen-analysis techniques [10]. The backscattering coefficient is expressed in terms of the incident and scattered Stokes vectors $\overline{I}_{0i}$ and $\overline{I}_{0s}$ as

$$\sigma_{\beta\alpha}(\theta_{0i}) = 4\pi \cos\theta_{0i} \frac{I_{0s\beta}(\theta_{0i}, \phi_{0i} + \pi)}{I_{0i\alpha}(\pi - \theta_{0i}, \phi_{0i})} \tag{6}$$

where α, β can be vertical (v) or horizontal (h) polarization, and the subscripts i and s denote the incident and scattered waves, respectively.

B. Thin Saline Ice Growth Model

The growth of sea ice is generally determined by both thermodynamic processes of freezing and melting and dynamic processes of ice drift and deformation [12,13]. However, a simplified growth model is applied in this study which neglects the ice drift and deformation. The ice freezing and melting processes are primarily influenced by heat and radiation exchanges between atmosphere and ocean. We use a one-dimensional thermodynamic model of sea ice developed in [1,15] to model the time-dependent thermodynamic processes occurring within the ice based on energy balance equations at the atmospheric and oceanic boundaries.

The balance of fluxes at the upper surface of the ice can be expressed as [1,13-15]

$$(1 - \alpha)F_r - F_{ri} + F_L - \varepsilon\sigma(T_s + 273)^4 + F_s + F_e + F_c = 0 \tag{7}$$

where the terms α and ε are the albedo and the long-wave emissivity of sea ice, respectively. σ is the Stefan-Boltzmann constant, and T_s is the ice surface temperature in $^\circ C$. In (7), F_r represents the downward short-wave radiation, and F_{ri} is the amount of short-wave energy that penetrates through the sea ice layer. The sum of F_r and F_{ri} gives the net flux of short-wave radiation absorbed in the interior of the ice layer. F_L is the downward long-wave insolation and $\varepsilon\sigma(T_s + 273)^4$ is the long-wave radiation emitted by the ice. These two

terms account for the net flux of long-wave energy. The two quantities F_s, the sensible heat flux, and F_e, the latent heat flux, represent the atmospheric turbulent heat fluxes which are related with the meteorological factors like air density, wind speed, humidity, and air temperature. The last term F_c in (7) is the upward conductive heat flux which is the heat from the bottom interface conducted through the ice to the upper surface.

At the bottom boundary of ice, by neglecting the contribution from oceanic heat flux, the conductive heat flux is related to the ice growth rate according to [12,15]

$$F_c = \rho L_f \frac{dh}{dt} \tag{8}$$

where h is the ice thickness, ρ is the density of sea ice, and L_f is the latent heat of freezing in $J\,kg^{-1}$.

Equations (7) and (8) are coupled via the heat conduction term F_c, whose solution generally requires the information about air and ice surface temperature, solar insolation, wind speed, humidity, etc. In this model, an approximation of ice albedo α is used [15]

$$\alpha = 0.44h^{0.28} + 0.08 \tag{9}$$

which is parameterized to be a function of ice thickness. ε is assumed to be unity in this study [1]. The short and long-wave fluxes F_r and F_L are acquired from the measurement as shown in Figure 2(a). F_{ri} is assumed to be 90% of the net short-wave radiation, i.e., $F_{ri} = 0.9(1-\alpha)F_r$, passes through the ice completely and is absorbed in the sea water.

Over the ice surface, the turbulent fluxes F_s and F_e are [1,13,15]

$$F_s = \rho_a C_p C_s u(T_a - T_s) \tag{10}$$

$$F_e = \rho_a L_v C_e u(q_a - q_s) \tag{11}$$

where ρ_a and C_p are the density and specific heat of the air, respectively. C_s is the transfer coefficient for sensible heat, T_a is the air temperature, T_s is the ice surface temperature, and u is the wind speed. L_v is the latent heat of vaporization, and C_e is the vaporation coefficient. The terms q_a and q_s in (11) are the specific humidities in the air and at the ice surface, respectively. The relation of $(q_a - q_b)$ given in [1] is used in this study. The relation is a parameterized function of air temperature, ice surface temperature, air pressure (p_0), and relative humidity (RH), which are all measurable quantities. Values of these parameters used in this study are given in Table 1.

Table 1: Model parameters for ice growth.

ρ_a	$1.3\ kg\,m^{-3}$	u	$0.60\ m\,s^{-1}$
C_p	$1006\ J\,kg^{-1}\,{}^{\circ}K^{-1}$	p_0	$1.013 \times 10^5\ N\,m^{-2}$
C_s	0.003	RH	0.8
C_e	0.00175	S_{i0}	$12.0\ {}^{0}/_{00}$
L_v	$2.5 \times 10^6\ J\,kg^{-1}$	d_s	$0.458\ {}^{0}/_{00}\,cm^{-1}$
ρ_i	$917\ kg\,m^{-3}$	T_m	$-1.0\ {}^{\circ}C$

The latent heat of freezing L_f required in solving (8) is obtained from an empirical formula given by Fukusako [16]

$$L_f = 4.187 \times 10^3 \left(79.68 - 0.505T_m - 0.0273S_i + 4.3115\frac{S_i}{T_m} + 8 \times 10^{-4}T_mS_i - 0.009T_m^2\right) \tag{12}$$

with T_m being the ice melting temperature in $^{\circ}C$ and S_i the salinity. In (8), the density of gas-free saline ice ρ is related to the ice temperature T_i in $^{\circ}C$ and the salinity S_i through the following equation [17]

$$\rho = \frac{\rho_i F_1(T_i)}{F_1(T_i) - \rho_i S_i F_2(T_i)} \tag{13}$$

here ρ_i is the pure ice density, and the explicit functional forms of F_1 and F_2 can be found in the work of Cox and Weeks [17]. As discussed in the previous section, the ice growth accompanies a brine loss, the bulk salinity of thin saline ice can be approximated by a monotonic decreasing function of ice thickness h and a desalination factor d_s as

$$S_i = S_{i0} - d_s h, \tag{14}$$

for 1 cm $< h <$ 10 cm. In the above equation, S_{i0} is the extrapolated salinity at $h =$ 0. Equations (7)-(14) form the model for thin saline ice growth under varying thermal conditions. Given the meteorological informations as well as the ice surface temperature, the conductive heat flux F_c can be calculated from (7) and the ice growth rate is solved via (8).

C. Ice and Brine Pocket Thermal Properties

Not only the ice thickness is influenced by the thermal variations, the sea ice density, brine volume fraction, brine permittivity, and brine inclusion size, which are directly related

to the scattering from sea ice, are also affected by the changing meteorological factors. From the ice density given in (13), the volume fraction f_v of brine inclusions is given as [17]

$$f_v = \frac{\rho_i S_i}{F_1(T_i) - \rho_i S_i F_2(T_i)}. \tag{15}$$

A linear temperature profile within the sea ice layer is assumed, and the ice temperature T_i is taken as the mean temperature within the layer. The brine permittivity is determined from the empirical formulas given by Stogryn and Desargant [19].

Through the freezing and melting processes, the size of brine pockets also changes with thermal variations. However, no relations have been found by us which directly relates the brine pocket size with temperature. In this study we assume that the number density of brine inclusions and their shape do not change during the course of ice growth. The ratios of the axes of brine pocket at different ice temperatures T_1 and T_2 are thus related to the ratio of the brine volume fraction at different temperatures via

$$\frac{a(T_1)}{a(T_2)} = \frac{b(T_1)}{b(T_2)} = \frac{c(T_1)}{c(T_2)} = \left[\frac{f_v(T_1)}{f_v(T_2)}\right]^{1/3} \tag{16}$$

Thus, given the salinity S_i and the semi-axes $a(T_1)$, $b(T_1)$, and $c(T_1)$ at a temperature T_1, (15) and (16) are used to calculate the brine size at other temperature T_2. However, in the present study, we assume that the roughness at the air-ice interface does not have a temperature dependence [11].

D. Comparison of Model Results with Experimental Data

Based on the growth model described in Section IIIB, we first simulate the evolution of ice growth under diurnal thermal cycles. The required solar radiation and the air and ice surface temperatures are acquired from Figure 2, additional relevant parameters for this simulation are supplied in Table 1. The simulation starts at an initial ice thickness of 1.0 cm, which corresponds to the local time of 10:15pm January 19, 1994. A finite difference scheme is used to calculate the increase of ice thickness at every 15-minute step. To simplify the growth simulation, the ice temperature T_i is set equal to the mean of the sea ice melting temperature T_m (at the interface of ice and saline water) and the air-ice interface temperature T_s. The simulated saline ice growth is represented by the continuous curve in Figure 1(a), which compares well with the measured ground truth.

Table 2: Parameters for simulation of backscattering coefficient.

T_0	$-4.8\ ^oC$	d_s	$0.458\ ^0/_{00}\ cm^{-1}$
$a(T_0)$	$0.018\ cm$	l	$2.50\ cm$
$b(T_0)$	$0.180\ cm$	s	$0.035\ cm$
$c(T_0)$	$0.225\ cm$	ϵ_i	$(3.15 + i0.002)\epsilon_o$
$S_i(T_0)$	$11.6\ ^0/_{00}$	ϵ_w	$(61.6 + i40.4)\epsilon_o$
$a:b:c$	$1:10:12.5$	h_1	$0.50\ cm$

Figure 5 presents the comparison between the model backscatter and the C-band radar measurements at different observation angles during the ice growth. The backscatter simulation also starts from the ice thickness at 1 cm. At this reference time, the ice temperature, defined as T_0, the brine pocket size, $a(T_0)$, $b(T_0)$, and $c(T_0)$, and ice bulk salinity S_i are given in Table 2. For this time-series simulation, the following parameters: background ice permittivity ϵ_i, saline water permittivity ϵ_w, surface correlation length l, rms height s, thickness of incubation layer h_1, and the ratio of semi-axes of brine pocket $a:b:c$, are assumed to be constant. Their values are also summarized in Table 2. The assumption of uniform shape of brine pocket is based on the experimental observation of approximately constant ratio between the co- and cross-polarization returns. The values of T_0, $a(T_0)$, $b(T_0)$, $c(T_0)$, given in Table 2, are chosen by justifying the model results with the measured data. However, other model parameters are subject to dynamic changes in the course of ice growth.

From Figures 5(a) and 5(b), the simulated backscattering coefficient shows a good agreement with the measured data in both magnitude and diurnal cycling variations. The backscatter is higher during the warming daytime and lower during the night, which is also correlated with the ice surface temperature measurement. The temperature drops in the nighttime which may cause more liquid in the brine pockets to be frozen. The volumetric change of water to ice decreases the total fractional volume of brine and the size of brine pocket. Therefore, the backscatter from saline ice reduces during the night. On the other hand, the warming temperature in the daytime increases both brine inclusion size and brine volume fraction, and results in an increase of backscatter. Figure 6 presents the simulated ice temperature T_i, brine volume, and brine pocket size versus elapsed time. The diurnal cycles in the brine volume and brine pocket size are synchronous with the cycles of measured backscatters.

IV. TIME SERIES ICE THICKNESS INVERSION

In a previous paper [8], we developed an ice thickness inversion algorithm which employes time-series radar measurements. The algorithm was applied to a set of indoor saline ice experimental data [9], and successfully retrieved the evolution of ice thickness under a constant growth condition [8]. It was found that by incorporating an ice thermodynamic model into the inversion algorithm, the thickness estimation can be constrained sufficiently to predict more accurate results. The use of time series data is also helpful for resolving the non-uniqueness and stability problems [8,20]. In this section, we further apply this algorithm to reconstruct the evolution of ice growth under diurnal thermal conditions using the time-series outdoor radar observations.

A. Inversion Algorithm

In the electromagnetic remote sensing of sea ice medium, the radiations are randomly scattered by its volume and surface inhomogeneities, and therefore the relation between the sea ice physical properties and radar measurement is non-linear. Generally, we can define a non-linear forward operator $\overline{F}$ which relates the data, sensor, environment, and medium's characteristics as follows:

$$\overline{\sigma}_i = \overline{F}(t_i, \overline{z}, \overline{x}) + \overline{e}_i \tag{17}$$

where $\overline{\sigma}_i$ represents radar data at the measurement time t_i, and $\overline{e}_i$ is the discrepancy between the observation and model response. The vector $\overline{x}$ denotes the set of pertinent model parameters of saline ice:

$$\overline{x} = [h_0, S_{i0}, d_s, a_0, l, s] \tag{18}$$

here $h_0 = h(t_0)$ is the ice thickness at time t_0 (a reference time) when the first set of data is taken, and $a_0 = a(t_0)$ the corresponding brine pocket size at this time. The other terms S_{i0}, d_s, l, and s have been defined in Section IIIB. The array $\overline{z}$ encompasses all the other known parameters. To solve $\overline{x}$ from equation (17), a non-linear least-squares approach can be used to minimize the error function between the observation and the model. Figure 7 summarizes the reconstruction algorithm using time-series radar data for the ice thickness. The retrieval steps are described in the following.

Given the initial guess of model parameters $\overline{x}$, the ice growth model first predicts the subsequent ice characteristics (a, b, c, f_v, ϵ_b, h) by using the specified time intervals between

the series of radar measurements, and the corresponding series of atmospheric and meteorological information (F_r, F_L, u, p_0, and RH), and the ice surface temperature T_s. Together with the sensor parameters, this set of time-series ice parameters will next be transformed into a series of predicted backscattering coefficients $\overline{F}$ based on our sea ice scattering model. The guessed model parameters $\overline{x}$ is corrected according to the difference $\overline{e}$ between the measured and predicted backscatter data by using the Levenberg-Marquardt optimization algorithm [21–23]. The procedure is repeated until the error threshold is reached. The inverted initial thickness h_0 is finally applied back to the growth model to obtain the evolution of ice thickness.

Since the entire series of actual measurements is utilized to minimize the square of error, the estimation actually takes into consideration both previous and subsequent information about the state of sea ice. In this way, the range of possible retrieved thicknesses from an initial trial thickness can be reduced and the retrieval may be robust to the discrepancy between model responses and measurements. This algorithm of using time series data has shown a better inversion of ice thickness than the estimates based on individual microwave data from CRRELEX 93 indoor experiment [8].

B. Reconstruction Results

The sets of sequentially measured HH and VV polarization radar data in Figure 3 are applied to retrieve the ice thickness by using the inversion algorithm described above. The initial thickness is the pertinent parameter to be inverted. The unknown model parameters are constrained within appropriate physical ranges which are given in Table 3. The constraints on S_{i0} and d_s are determined by referencing the measured ground truth and the findings in published literature. On the other hand, the constraints on model parameters: a_0, l, and s are chosen based on our forward model simulations. The final inverted values of model parameters using co-polarization radar data at 30° and 40° incidence angles are given in Table 4, and the corresponding reconstructed ice thicknesses are shown in Figures 8(a) and 8(b), respectively. It is noted that the retrieved ice thickness agrees very well with the measured ice growth. Their respective rms errors are 0.373cm and 0.378cm.

Instead of using polarimetric data, we also apply the same algorithm but using single polarization time series data for the thickness retrieval, because presently many available remote sensing sensors are with either VV polarization (ERS) or HH polarization (RADARSAT) exclusively. For the single polarization cases, the unknown parameters and

Table 3: Initial guesses, lower constraints, and upper constraints of model parameters.

model parameters	initial guess	lower limit	upper limit
h_0 (cm)	0.50	0.50	4.50
a_0 (cm)	0.018	0.017	0.030
S_{i0} ($^0/_{00}$)	12.0	11.0	13.0
d_s ($^0/_{00}$/cm)	0.45	0.30	0.55
l (cm)	2.50	2.00	3.00
s (cm)	0.035	0.030	0.040

Table 4: Final inverted values of model parameters for different incidence angles and different polarizations.

model parameters	30°			40°		
	HH & VV	HH	VV	HH & VV	HH	VV
h_0 (cm)	0.59	0.62	0.64	0.62	0.63	0.73
a_0 (cm)	0.0171	0.0170	0.0181	0.0170	0.0172	0.0172
S_{i0} ($^0/_{00}$)	13.0	13.0	12.8	13.0	11.0	13.0
d_s ($^0/_{00}$/cm)	0.30	0.30	0.30	0.30	0.52	0.30
l (cm)	2.02	2.03	2.66	3.00	3.00	2.73
s (cm)	0.033	0.030	0.040	0.030	0.030	0.033

limits are the same as before. Table 4 gives the final inverted values of model parameters using either HH or VV polarization radar data at 30° and 40° incidence angles. Figures 9(a) and 9(b) illustrate the respective inversion results of ice thickness evolution. The retrieved ice thickness from single polarization data also shows reasonable agreement with the measured ground truth. Their rms errors are 0.267cm and 0.339cm for HH and VV polarization, respectively, at 30° incident angle, and 0.860cm (HH) and 0.407cm (VV) at 40° incident angle. The retrieved thickness from HH polarization data at 40° has a larger discrepancy compared with the ground truth, this may be due to the larger noisy level for the HH polarization at 40° which degraded the inversion result.

The thickness inversion presented above is subject to the time-series meteorological observations. Solar radiations and air temperature are required to deduce the surface fluxes. In lieu of supplied radiation measurements, we thus modify the inverse model such that the model provides estimates of solar radiations and air temperature on an average basis. Actually, in the polar areas these monthly-averaged estimates may be available in the literature [15]. In the following inverse scattering simulations, we instead use some estimated constant values for daily solar radiations and air temperatures: 400 W/m^2 for short-wave and 250 W/m^2 for long-wave solar radiations in the daytime, and 0 W/m^2 and 200 W/m^2 in the night, respectively; and $-10°C$ for the air temperature during the daytime and $-30°C$ during night. The wind speed is kept to be a constant of 0.6 m/s. The estimated constant values of solar radiations are chosen to give the same total energy when integrates the radiations shown in Figure 2(a) over time for day or night. The temperatures are chosen as the mean temperatures during day and night. With these estimated parameters, the retrieved ice thicknesses are shown in Figures 10(a) and 10(b) by using 30° incidence angle measurements and 40° incidence angle measurements, respectively. The rms errors for these retrievals are 0.284cm, 0.593cm, 0.396cm by using the 30° incidence angle measurements of HH-, VV-, and HH & VV polarization, respectively, and 0.812cm (HH), 0.308cm (VV), and 0.394cm (HH & VV) for the case of 40° incidence angle.

V. SUMMARY

The thermal interaction between sea ice and atmosphere strongly affects the thermodynamic processes associated with the ice growth. The thermally-induced varying ice physical properties also significantly influence the electromagnetic interactions with the sea ice medium. In this paper, we extend our previously developed sea ice inverse scattering model to further investigate the retrieval of ice thickness under diurnal thermal cycling conditions.

We use a one-dimensional thermodynamic model that includes thermal interactions with atmosphere for the ice growth using measured or estimated solar insolations and air temperatures. We provide a physically-based sea ice electromagnetic model with a multilayer random medium structure with rough surfaces, which can take into account the dynamically varying thermal and electromagnetic properties of saline ice and the combined volume and surface scattering effects. The direct scattering model interprets the large diurnal variations in the radar backscatter observed in the CRRELEX 94 experiment. By using the same set of data, the developed inversion algorithm has successfully reconstructs the evolution of ice growth under a thermal cycling environment. The good agreement between the reconstructed ice thickness and ground-based measurements confirms the usefulness of incorporating ice growth physics and using time series data in the electromagnetic inverse scattering problem of sea ice.

ACKNOWLEDGMENT

The research in this paper was partially supported by the Office of Naval Research Contract No. N00014-92-J-4098 with the Massachusetts Institute of Technology. The research performed by the Center for Space Microelectronics Technology, Jet Propulsion Laboratory, California Institute of Technology was supported by the Office of Naval Research through an agreement with the National Aeronautics and Space Administration.

APPENDIX

In this appendix, we give the reflection matrix $\overline{\overline{R}}_{\alpha\beta}(\theta,\phi;\theta',\phi')$, and transmission matrix $\overline{\overline{T}}_{\alpha\beta}(\theta,\phi;\theta',\phi')$ for a slightly rough interface between α-th and β-th layers. Each matrix can be separated into two terms; coherent and incoherent:

$$\begin{aligned}\overline{\overline{R}}_{\alpha\beta}(\theta,\phi;\theta',\phi') &= \overline{\overline{R}}^{c}_{\alpha\beta}(\theta,\phi)\delta(\phi-\phi')\delta(\cos\theta-\cos\theta') \\ &+ \overline{\overline{R}}^{i}_{\alpha\beta}(\theta,\phi;\theta',\phi') \qquad \text{(A.1)} \\ \overline{\overline{T}}_{\alpha\beta}(\theta,\phi;\theta',\phi') &= \overline{\overline{T}}^{c}_{\alpha\beta}(\theta,\phi)\delta(\phi-\phi')\delta(\cos\theta-\cos\theta') \\ &+ \overline{\overline{T}}^{i}_{\alpha\beta}(\theta,\phi;\theta',\phi') \qquad \text{(A.2)}\end{aligned}$$

The coherent matrices have the following form:

$$\overline{\overline{R}}^{c}_{\alpha\beta}(\theta_\alpha) = \begin{bmatrix} |S_{\alpha\beta}|^2 & 0 & 0 & 0 \\ 0 & |W_{\alpha\beta}|^2 & 0 & 0 \\ 0 & 0 & \mathrm{Re}(S_{\alpha\beta}W^*_{\alpha\beta}) & -\mathrm{Im}(S_{\alpha\beta}W^*_{\alpha\beta}) \\ 0 & 0 & \mathrm{Im}(S_{\alpha\beta}W^*_{\alpha\beta}) & \mathrm{Re}(S_{\alpha\beta}W^*_{\alpha\beta}) \end{bmatrix} \tag{A.3}$$

$$\overline{\overline{T}}^{c}_{\alpha\beta}(\theta_\alpha) = \frac{\epsilon'_\beta \cos(\theta_\beta)}{\epsilon'_\alpha \cos(\theta_\alpha)} \begin{bmatrix} |Y_{\alpha\beta}|^2 & 0 & 0 & 0 \\ 0 & |X_{\alpha\beta}|^2 & 0 & 0 \\ 0 & 0 & \mathrm{Re}(Y_{\alpha\beta}X^*_{\alpha\beta}) & -\mathrm{Im}(Y_{\alpha\beta}X^*_{\alpha\beta}) \\ 0 & 0 & \mathrm{Im}(Y_{\alpha\beta}X^*_{\alpha\beta}) & \mathrm{Re}(Y_{\alpha\beta}X^*_{\alpha\beta}) \end{bmatrix} \tag{A.4}$$

where

$$\begin{aligned} W_{\alpha\beta} &= R_h + k_{\alpha zi}\frac{(k_\beta^2 - k_\alpha^2)}{(k_{\alpha zi} + k_{\beta zi})^2}\sigma^2 l^2 \int_0^\infty k_\rho dk_\rho \exp\left[-\frac{1}{4}(k_\rho^2 + k_{\rho i}^2)l^2\right] \\ &\cdot \left\{\left[-\frac{k_\beta^2 - k_\alpha^2}{k_{\alpha z} + k_{\beta z}}\frac{k_{\alpha z}k_{\beta z}}{k_{\alpha z}k_{\beta z} + k_\rho^2} + k_{\beta zi}\right] I_0(x) \right. \\ &\left. -\frac{k_\beta^2 - k_\alpha^2}{k_{\alpha z} + k_{\beta z}}\frac{k_\rho^2}{k_{\alpha z}k_{\beta z} + k_\rho^2}\left[I_0(x) - \frac{I_1(x)}{x}\right]\right\} \end{aligned} \tag{A.5}$$

$$\begin{aligned} S_{\alpha\beta} &= R_v - k_{\alpha zi}\frac{(k_\beta^2 - k_\alpha^2)}{(k_\alpha^2 k_{\beta zi} + k_\beta^2 k_{\alpha zi})^2}k_\alpha^2 k_\beta^2 \sigma^2 l^2 \int_0^\infty k_\rho dk_\rho \exp\left[-\frac{1}{4}(k_\rho^2 + k_{\rho i}^2)l^2\right] \\ &\cdot \left\{k_{\beta zi}\left[I_0(x) - 2\frac{k_\rho k_{\rho i}}{k_{\alpha z}k_{\beta z} + k_\rho^2}I_1(x)\right] - \frac{k_\beta^2 - k_\alpha^2}{k_{\alpha z} + k_{\beta z}}\frac{k_{\beta zi}^2}{k_\beta^2}I_0(x) \right. \\ &+ \frac{k_\beta^2 - k_\alpha^2}{k_{\alpha z} + k_{\beta z}}\frac{k_{\beta zi}^2}{k_\beta^2}\frac{k_\rho^2}{k_{\alpha z}k_{\beta z} + k_\rho^2}\cdot\left[I_0(x) - \frac{I_1(x)}{x}\right] \\ &\left. - \frac{k_\beta^2 - k_\alpha^2}{k_{\alpha z} + k_{\beta z}}\frac{k_\rho^2 k_{\rho i}^2}{k_{\alpha z}k_{\beta z} + k_\rho^2}\frac{1}{k_\alpha^2}I_0(x)\right\} \end{aligned} \tag{A.6}$$

$$\begin{aligned} X_{\alpha\beta} &= 1 + R_h + k_{\alpha zi}\frac{(k_\beta^2 - k_\alpha^2)}{(k_{\alpha zi} + k_{\beta zi})^2}\sigma^2 l^2 \int_0^\infty k_\rho dk_\rho \exp\left[-\frac{1}{4}(k_\rho^2 + k_{\rho i}^2)l^2\right] \\ &\cdot \left\{(k_{\alpha z} - k_{\beta z})\left[I_0(x) - \frac{k_\rho^2}{k_{\alpha z}k_{\beta z} + k_\rho^2}\frac{I_1(x)}{x}\right] - \frac{1}{2}(k_{\alpha zi} - k_{\beta zi})I_0(x)\right\} \end{aligned} \tag{A.7}$$

$$\begin{aligned} Y_{\alpha\beta} &= 1 + R_v + k_{\alpha zi}\frac{(k_\beta^2 - k_\alpha^2)}{(k_\alpha^2 k_{\beta zi} + k_\beta^2 k_{\alpha zi})^2}k_\beta^2 \sigma^2 l^2 \int_0^\infty k_\rho dk_\rho \exp\left[-\frac{1}{4}(k_\rho^2 + k_{\rho i}^2)l^2\right] \\ &\cdot \left\{-\frac{1}{2}(k_\alpha^2 k_{\beta zi} - k_\beta^2 k_{\alpha zi})I_0(x) - (k_\beta^2 - k_\alpha^2)\frac{k_\rho^2 k_{\rho i}^2}{k_\alpha^2 k_{\beta z} + k_\beta^2 k_{\alpha z}}I_0(x) \right. \\ &- \frac{k_\beta^2 - k_\alpha^2}{k_{\alpha z} + k_{\beta z}}k_{\alpha zi}k_{\beta zi}I_0(x) + (k_\beta^2 - k_\alpha^2)\frac{k_\rho^2 k_{\alpha zi}k_{\beta zi}}{k_\alpha^2 k_{\beta z} + k_\beta^2 k_{\alpha z}}\left[I_0(x) - \frac{I_1(x)}{x}\right] \end{aligned}$$

$$+\frac{k_{\alpha z}+k_{\beta z}}{k_\alpha^2 k_{\beta z}+k_\beta^2 k_{\alpha z}} k_\rho k_{\rho i}(k_\alpha^2 k_{\beta z i}-k_\beta^2 k_{\alpha z i}) I_1(x)\Bigg\} \tag{A.8}$$

In the above equations, R_h and R_v are the TE and TM Fresnel reflection coefficients, $x = \frac{1}{2}k_\rho k_{\rho i} l^2$, and I_0 and I_1 are the zeroth- and first-order modified Bessel functions, respectively.

The incoherent matrices which can be obtained for the first order SPM solution are given by:

$$\overline{\overline{R}}^i_{\alpha\beta} = \begin{bmatrix} \langle|f^r_{vv}|^2\rangle & \langle|f^r_{vh}|^2\rangle \\ \langle|f^r_{hv}|^2\rangle & \langle|f^r_{hh}|^2\rangle \\ 2\mathrm{Re}(\langle f^r_{vv} {f^r_{hv}}^*\rangle) & 2\mathrm{Re}(\langle f^r_{vh} {f^r_{hh}}^*\rangle) \\ 2\mathrm{Im}(\langle f^r_{vv} {f^r_{hv}}^*\rangle) & 2\mathrm{Im}(\langle f^r_{vh} {f^r_{hh}}^*\rangle) \end{bmatrix}$$
$$\begin{bmatrix} \mathrm{Re}(\langle f^r_{vv} {f^r_{vh}}^*\rangle) & -\mathrm{Im}(\langle f^r_{vv} {f^r_{vh}}^*\rangle) \\ \mathrm{Re}(\langle f^r_{hv} {f^r_{hh}}^*\rangle) & -\mathrm{Im}(\langle f^r_{hv} {f^r_{hh}}^*\rangle) \\ \mathrm{Re}(\langle f^r_{vv} {f^r_{hh}}^* + f^r_{vh} {f^r_{hv}}^*\rangle) & -\mathrm{Im}(\langle f^r_{vv} {f^r_{hh}}^* - f^r_{vh} {f^r_{hv}}^*\rangle) \\ \mathrm{Im}(\langle f^r_{vv} {f^r_{hh}}^* + f^r_{vh} {f^r_{hv}}^*\rangle) & \mathrm{Re}(\langle f^r_{vv} {f^r_{hh}}^* - f^r_{vh} {f^r_{hv}}^*\rangle) \end{bmatrix} \tag{A.9}$$

$$\overline{\overline{T}}^i_{\alpha\beta} = \begin{bmatrix} \langle|f^t_{vv}|^2\rangle & \langle|f^t_{vh}|^2\rangle \\ \langle|f^t_{hv}|^2\rangle & \langle|f^t_{hh}|^2\rangle \\ 2\mathrm{Re}(\langle f^t_{vv} {f^t_{hv}}^*\rangle) & 2\mathrm{Re}(\langle f^t_{vh} {f^t_{hh}}^*\rangle) \\ 2\mathrm{Im}(\langle f^t_{vv} {f^t_{hv}}^*\rangle) & 2\mathrm{Im}(\langle f^t_{vh} {f^t_{hh}}^*\rangle) \end{bmatrix}$$
$$\begin{bmatrix} \mathrm{Re}(\langle f^t_{vv} {f^t_{vh}}^*\rangle) & -\mathrm{Im}(\langle f^t_{vv} {f^t_{vh}}^*\rangle) \\ \mathrm{Re}(\langle f^t_{hv} {f^t_{hh}}^*\rangle) & -\mathrm{Im}(\langle f^t_{hv} {f^t_{hh}}^*\rangle) \\ \mathrm{Re}(\langle f^t_{vv} {f^t_{hh}}^* + f^t_{vh} {f^t_{hv}}^*\rangle) & -\mathrm{Im}(\langle f^t_{vv} {f^t_{hh}}^* - f^t_{vh} {f^t_{hv}}^*\rangle) \\ \mathrm{Im}(\langle f^t_{vv} {f^t_{hh}}^* + f^t_{vh} {f^t_{hv}}^*\rangle) & \mathrm{Re}(\langle f^t_{vv} {f^t_{hh}}^* - f^t_{vh} {f^t_{hv}}^*\rangle) \end{bmatrix} \tag{A.10}$$

where

$$\langle f^\gamma_{pq} {f^\gamma_{uw}}^*\rangle = (g^\gamma_{pq})\cdot(g^\gamma_{uw})^* \qquad \gamma = r,t \ \ and \ \ p,q,u,w = h,v \tag{A.11}$$

and

$$g^r_{vv} = m^r(\theta_s,\theta_i)\Bigg\{\frac{(k_\beta^2-k_\alpha^2)}{(k_\alpha^2 k_{\beta z}+k_\beta^2 k_{\alpha z})(k_\alpha^2 k_{\beta z i}+k_\beta^2 k_{\alpha z i})}\Big[k_\alpha^2 k_\beta^2 \sin\theta_s \sin\theta_i - k_\alpha^2 k_{\beta z} k_{\beta z i}\cos(\phi_s-\phi_i)\Big]\Bigg\} \tag{A.12}$$

$$g^r_{vh} = \zeta\cdot m^r(\theta_s,\theta_i)\Bigg\{\frac{(k_\beta^2-k_\alpha^2)k_\alpha k_{\beta z}}{(k_\alpha^2 k_{\beta z}+k_\beta^2 k_{\alpha z})(k_{\alpha z i}+k_{\beta z i})}\Bigg\}\sin(\phi_s-\phi_i) \tag{A.13}$$

$$g^r_{hv} = \zeta\cdot m^r(\theta_s,\theta_i)\Bigg\{\frac{(k_\beta^2-k_\alpha^2)k_\alpha k_{\beta z i}}{(k_\alpha^2 k_{\beta z i}+k_\beta^2 k_{\alpha z i})(k_{\alpha z}+k_{\beta z})}\Bigg\}\sin(\phi_s-\phi_i) \tag{A.14}$$

$$g^r_{hh} = m^r(\theta_s,\theta_i)\Bigg\{\frac{(k_\beta^2-k_\alpha^2)}{(k_{\alpha z}+k_{\beta z})(k_{\alpha z i}+k_{\beta z i})}\Bigg\}\cos(\phi_s-\phi_i) \tag{A.15}$$

and

$$g^t_{vv} = m^t(\theta_t,\theta_i)\left\{\frac{(k_\beta^2-k_\alpha^2)k_\alpha k_\beta}{(k_\alpha^2 k_{\beta z}+k_\beta^2 k_{\alpha z})(k_\alpha^2 k_{\beta zi}+k_\beta^2 k_{\alpha zi})}[k_\alpha k_\beta \sin\theta_t \sin\theta_i - k_{\alpha z}k_{\beta zi}\cos(\phi_t-\phi_i)]\right\} \quad \text{(A.16)}$$

$$g^t_{vh} = -\zeta\cdot m^t(\theta_t,\theta_i)\left\{\frac{(k_\beta^2-k_\alpha^2)k_\beta k_{\alpha z}}{(k_\alpha^2 k_{\beta z}+k_\beta^2 k_{\alpha z})(k_{\alpha zi}+k_{\beta zi})}\right\}\sin(\phi_t-\phi_i) \quad \text{(A.17)}$$

$$g^t_{hv} = \zeta\cdot m^t(\theta_t,\theta_i)\left\{\frac{(k_\beta^2-k_\alpha^2)k_\alpha k_{\beta zi}}{(k_\alpha^2 k_{\beta zi}+k_\beta^2 k_{\alpha zi})(k_{\alpha z}+k_{\beta z})}\right\}\sin(\phi_t-\phi_i) \quad \text{(A.18)}$$

$$g^t_{hh} = m^t(\theta_t,\theta_i)\left\{\frac{(k_\beta^2-k_\alpha^2)}{(k_{\alpha z}+k_{\beta z})(k_{\alpha zi}+k_{\beta zi})}\right\}\cos(\phi_t-\phi_i) \quad \text{(A.19)}$$

with

$$|m^r(\theta_s,\theta_i)|^2 = \frac{k_\alpha^4\sigma^2 l^2\cos\theta_s\cos^2\theta_i}{\pi} e^{-1/4(\sin^2\theta_s+\sin^2\theta_i)k_\alpha^2 l^2} \cdot e^{1/2(\sin\theta_s\cdot\sin\theta_i)k_\alpha^2 l^2\cos(\phi_s-\phi_i)} \quad \text{(A.20)}$$

$$|m^t(\theta_t,\theta_i)|^2 = \frac{\eta_\alpha k_\alpha^2 k_\beta^2\sigma^2 l^2\cos\theta_t\cos^2\theta_i}{\eta_\beta\pi} e^{-1/4(k_\beta^2\sin^2\theta_t+k_\alpha^2\sin^2\theta_i)l^2} \cdot e^{1/2(\sin\theta_t\cdot\sin\theta_i)k_\alpha k_\beta l^2\cos(\phi_t-\phi_i)} \quad \text{(A.21)}$$

where η is the medium impedance and $\zeta = 1$ when the incident wave propagates in the downward direction and $\zeta = -1$ when the incident wave propagates in the upward direction.

REFERENCES

[1] G.A. Maykut, "Energy exchange over young sea ice in the central Arctic," *J. Geophys. Res.*, vol. 83, no. C7, pp. 3646–3658, 1978.

[2] F.D. Carsey, ed., *Microwave Remote Sensing of Sea Ice*, DC: American Geophysical Union, 1992.

[3] F.T. Ulaby, R.K. Moore, and A.K. Fung, *Microwave Remote Sensing, Vol. I and II*, Reading, MA: Addison-Wesley, 1982.

[4] S.V. Nghiem, R. Kwok, S.H. Yueh, and M.R. Drinkwater, "Polarimetric signature of sea ice, 2. Experimental observations," *J. Geophys. Res.*, vol. 100, no. C7, pp. 13681–13698, 1995.

[5] R. Kwok, E. Rignot, B. Holt, and R. Onstott, "Identification of sea ice types in spaceborne synthetic aperture radar data," *J. Geophys. Res.*, vol. 97, no. C2, pp. 2391–2402, 1992.

[6] D.P. Winebrenner, L.D. Farmer, and I.R. Joughin, "On the response of polarimetric synthetic aperture radar signatures at 24-cm wavelength to sea ice thickness in Arctic leads," *Radio Sci.*, vol. 30, no. 2, pp. 373–402, 1995.

[7] R. Kwok, S.V. Nghiem, S.H. Yueh, and D.D. Huynh, "Retrieval of thin ice thickness from multifrequency polarimetric SAR data," *Remote Sens. Environ.*, vol.51, no. 3, pp. 361–374, 1995.

[8] S.E. Shih, K.H. Ding, S.V. Nghiem, C.C. Hsu, J.A. Kong, and A.K. Jordan, "Thin saline ice thickness retrieval using time series C-band polarimetric radar measurements," *IEEE Trans. Geosci. Remote Sens.*, in press, 1998.

[9] S.V. Nghiem, R. Kwok, S.H. Yueh, A.J. Gow, D.K. Perovich, J.A. Kong, and C.C. Hsu, "Evolution in polarimetric signatures of thin saline ice under constant growth," *Radio Sci.*, vol. 32, no. 1, pp. 127–151, 1997.

[10] L. Tsang, J.A. Kong, and R.T. Shin, *Theory of Microwave Remote Sensing*, New York: Wiley-Interscience, 1985.

[11] S.V. Nghiem, R. Kwok, S.H. Yueh, A.J. Gow, D.K. Perovich, C.C. Hsu, K.H. Ding, J.A. Kong, and T.C. Grenfell, "Diurnal thermal cycling effects on microwave signatures of thin sea ice," *IEEE Trans. Geosci. Remote Sens.*, vol. 36, no. 1, pp. 111–124, 1998.

[12] W.F. Weeks and S.F. Ackley, *The Growth, Structure, and Properties of Sea Ice, CRREL Monograph 82-1*, US Army Corps of Eng., Cold Regions Research and Engineering Lab., 1982.

[13] G.A. Maykut, "The surface heat and mass balance," *The Geophysics of Sea Ice*, Chapter 5, pp. 395–463, N. Untersteiner ed., New York: Plenum Press, 1986.

[14] G.F.N. Cox and W.F. Weeks, "Numerical simulations of the profile properties of undeformed first-year sea ice during the growth season," *J. Geophys. Res.*, vol. 93, no. C10, pp. 12449–12460, 1988.

[15] G.A. Maykut, "Large-scale heat exchange and ice production in the central Arctic," *J. Geophys. Res.*, vol. 87, no. C10, pp. 7971–7984, 1982.

[16] S. Fukusako, "Thermophysical properties of ice, snow, and sea ice," *Int. J. Thermophys.*, vol. 11, no. 2, pp. 353–372, 1990.

[17] G.F.N. Cox and W.F. Weeks, "Equations for determining the gas and brine volumes in sea-ice samples," *J. Glaciol.*, vol. 29, no. 102, pp. 306–316, 1983.

[18] L.A. Klein and C. Swift, "An improved model for the dielectric constant of sea water at microwave frequencies," *IEEE Trans. Antennas Propagat.*, vol. AP-25, no. 1, pp. 104–111, 1977.

[19] A. Stogryn and G.J. Desargant, "The dielectric properties of brine in sea ice at microwave frequencies," *IEEE Trans. Antennas Propagat.*, vol. AP-33, no. 5, pp. 523–532, 1985.

[20] A.K. Jordan and M.E. Veysoglu, "Electromagnetic remote sensing of sea ice," *Inverse Problems*, vol. 10, no. 5, pp. 1041–1058, 1994.

[21] D.W. Marquardt, "An algorithm for least-squares estimation of nonlinear parameters," *J. Soc. Indust. Appl. Math.*, vol. 11, pp. 431–441, 1963.

[22] J.L. Kuester and J.H. Mize, *Optimization Techniques with Fortran*, New York: McGraw-Hill, 1973.

[23] J.E. Dennis and R.B. Schnabel, *Numerical Methods for Unconstrained Optimization and Nonlinear Equations*, Englewood Cliffs, NJ: Prentice-Hall, 1983.

Figure Captions

Figure 1. Ground-based ice characteristic measurements from CRRELEX 94 outdoor saline ice experiment. (a) Ice thickness versus time. Solid curve is the simulation of saline ice growth. (b) Saline ice bulk salinity versus thickness. Solid line is the linear fit of measured data.

Figure 2. Ground-based measurements of solar radiations and air and ice surface temperatures from CRRELEX 94 outdoor saline ice experiment. (a) Short-wave (0.3–3 μm) and long-wave (3–50 μm) solar radiation. (b) Air and ice surface temperatures.

Figure 3. Polarimetric backscattering coefficients and ice surface temperature as a function of ice thickness. (a) 30° incident angle. (b) 40° incident angle. V and H stand for measured data for VV- and HH-polarization, respectively. Circles represnt the measured ice surface temperature.

Figure 4. Geometric model configuration of saline ice. The uppermost medium is air with permittivity ϵ_o, the lower half space is saline water with complex permittivity ϵ_w, and the middle two layers of thicknesses h_1 and h_2 represent the saline ice. Within the ice layers, the background is pure ice with complex permittivity ϵ_i, brine inclusions are modeled as randomly distributed ellipsoids with complex permittivity ϵ_{b1} and ϵ_{b2}. Top rough interface is characterized by the correlation length l and height variation s. Other interfaces are flat surfaces.

Figure 5. Comparisons of the measured and model backscattering coefficients. (a) 30° incidence angle. (b) 40° incidence angle. H, X, and V stand for measured data in HH-, HV-, and VV-polarization, respectively. The corresponding model simulation results are represented by solid, dashed, and dot-dashed curves, respectively.

Figure 6. Simulated ice bulk properties as a function of time in the course of ice growth. (a) Ice temperature T_i in $°C$. (b) Brine volume fraction. (c) Bine pocket size a in cm.

Figure 7. Block diagram of the inversion algorithm using time series measured data. The dynamic electromagnetic scattering model which includes a electromagnetic scattering model and an ice growth model is enclosed by a dashed rectangle.

Figure 8. Thickness retrieval using both HH & VV time series data. (a) 30° incidence angle. (b) 40° incidence angle. o represents the measured ice thickness. Solid curve indicates the

evolution of reconstructed ice thickness using measured time series data.

Figure 9. Thickness retrieval using single polarization time series data. (a) 30° incidence angle. (b) 40° incidence angle. o represents the measured ice thickness. Solid curve indicates the evolution of reconstructed ice thickness using measured HH-polarization time series data; dashed curve indicates the evolution of reconstructed ice thickness using measured VV-polarization time series data.

Figure 10. Thickness retrieval using solar radiations and air temperatures. (a) 30° incidence angle. (b) 40° incidence angle. o represents the measured ice thickness. Solid curve indicates the evolution of reconstructed ice thickness using measured both HH & VV time series data; dashed curve indicates the evolution of reconstructed ice thickness using measured HH-polarization time series data; dotted curve indicates the evolution of reconstructed ice thickness using measured VV-polarization time series data.

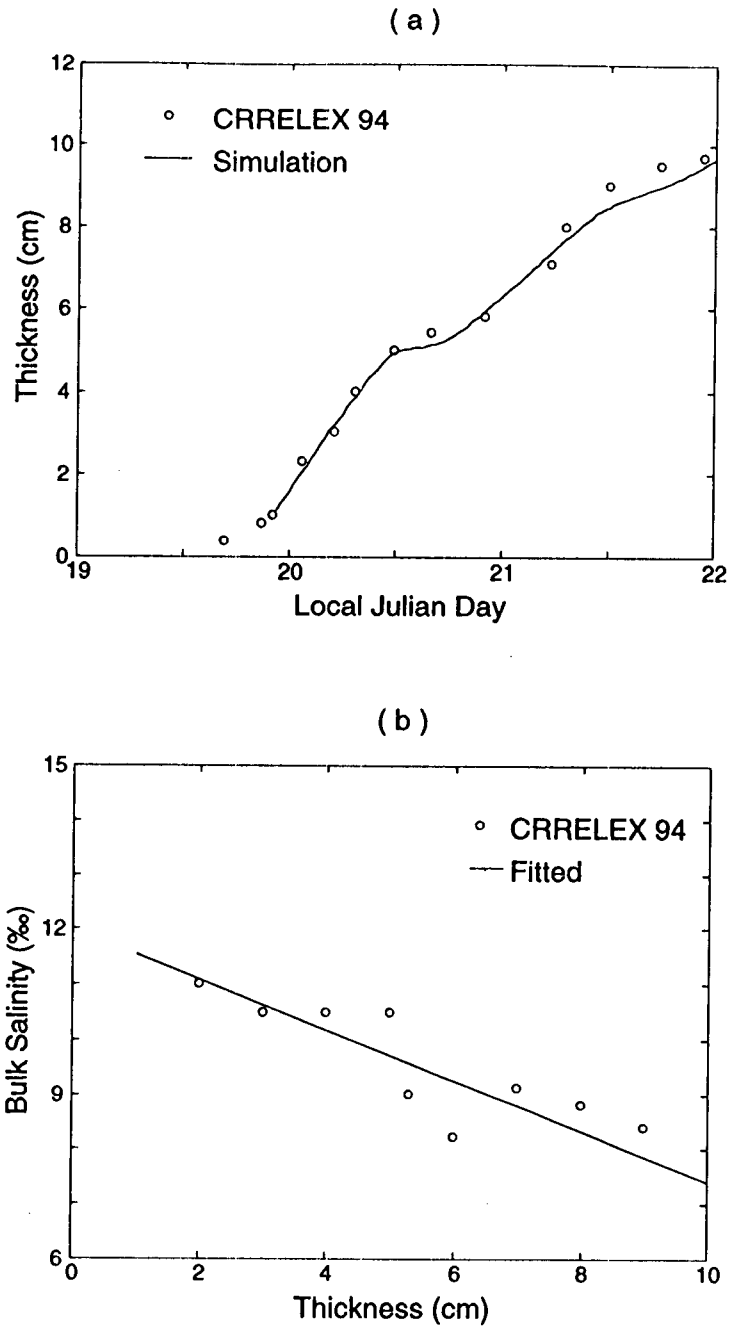

Figure 1: Ground-based ice characteristic measurements from CRRELEX 94 outdoor saline ice experiment. (a) Ice thickness versus time. Solid curve is the simulation of saline ice growth. (b) Saline ice bulk salinity versus thickness. Solid line is the linear fit of measured data.

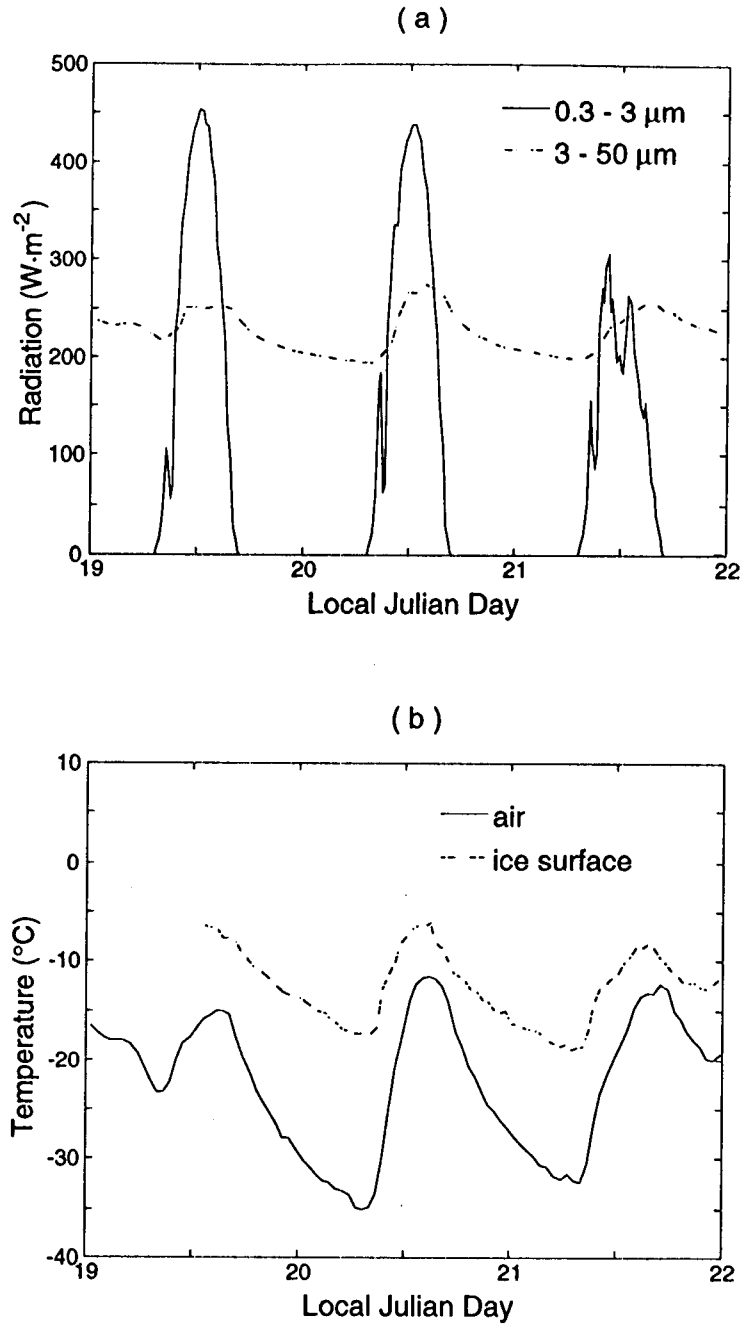

Figure 2: Ground-based measurements of solar radiations and air and ice surface temperatures from CRRELEX 94 outdoor saline ice experiment. (a) Short-wave (0.3–3 μm) and long-wave (3–50 μm) solar radiation. (b) Air and ice surface temperatures.

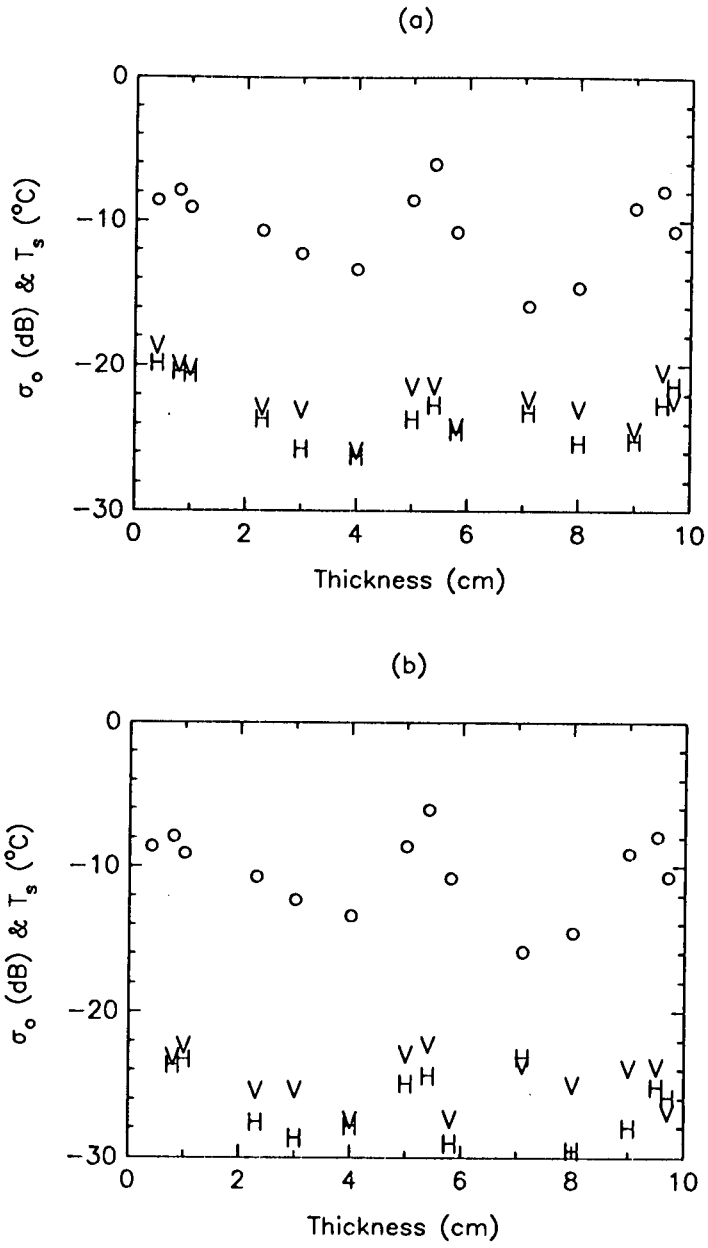

Figure 3: Polarimetric backscattering coefficients and ice surface temperature as a function of ice thickness. (a) 30° incident angle. (b) 40° incident angle. V and H stand for measured data for VV- and HH-polarization, respectively. Circles represnt the measured ice surface temperature.

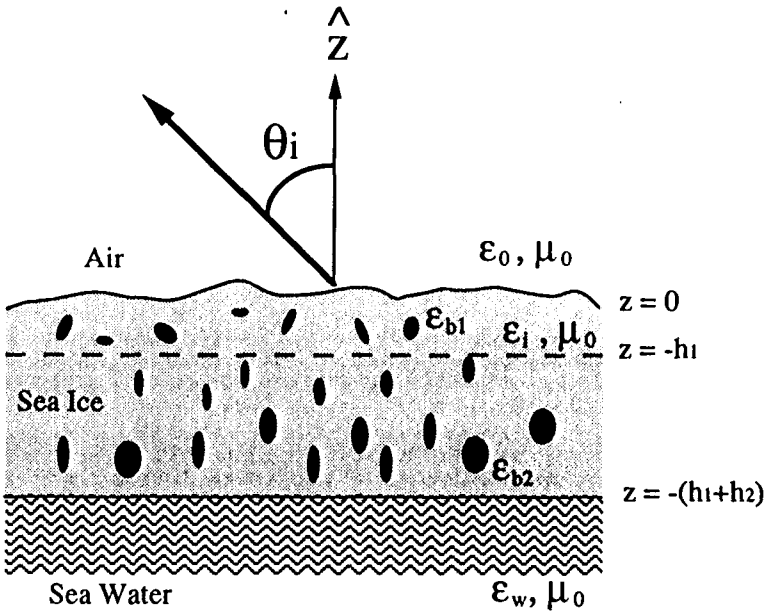

Figure 4: Geometric model configuration of saline ice. The uppermost medium is air with permittivity ϵ_o, the lower half space is saline water with complex permittivity ϵ_w, and the middle two layers of thicknesses h_1 and h_2 represent the saline ice. Within the ice layers, the background is pure ice with complex permittivity ϵ_i, brine inclusions are modeled as randomly distributed ellipsoids with complex permittivity ϵ_{b1} and ϵ_{b2}. Top rough interface is characterized by the correlation length l and height variation s. Other interfaces are flat surfaces.

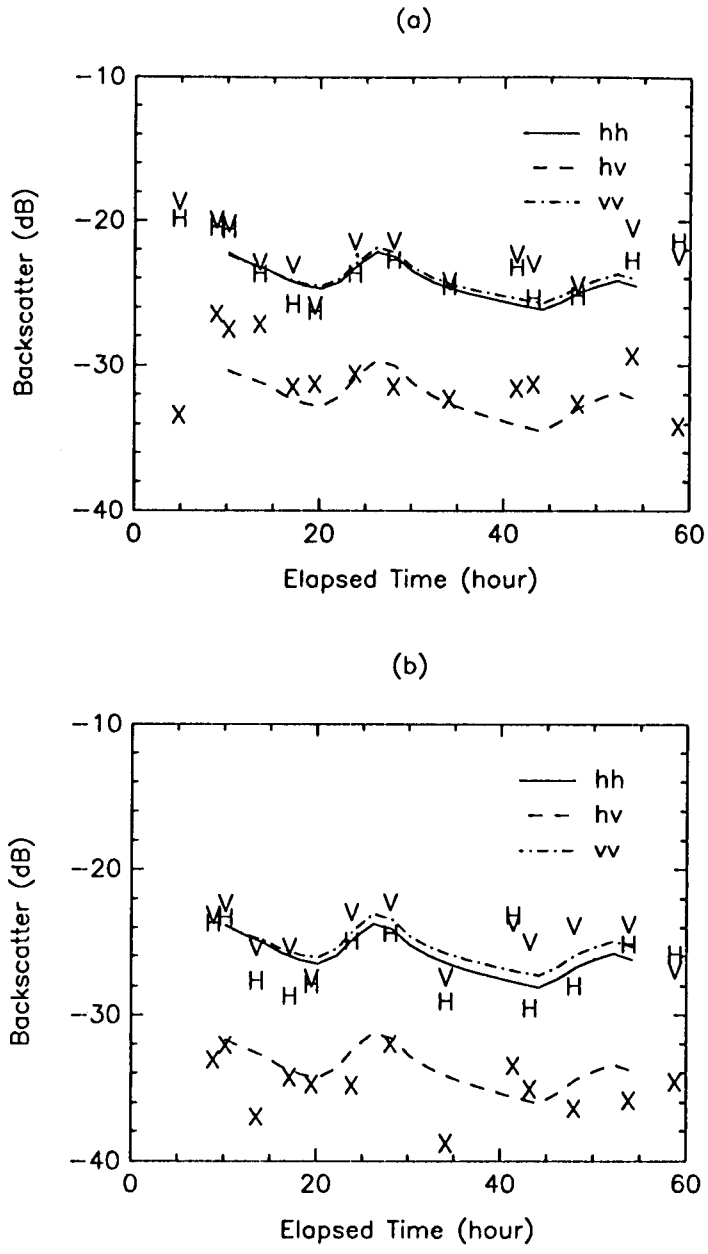

Figure 5: Comparisons of the measured and model backscattering coefficients. (a) 30° incidence angle. (b) 40° incidence angle. H, X, and V stand for measured data in HH-, HV-, and VV-polarization, respectively. The corresponding model simulation results are represented by solid, dashed, and dot-dashed curves, respectively.

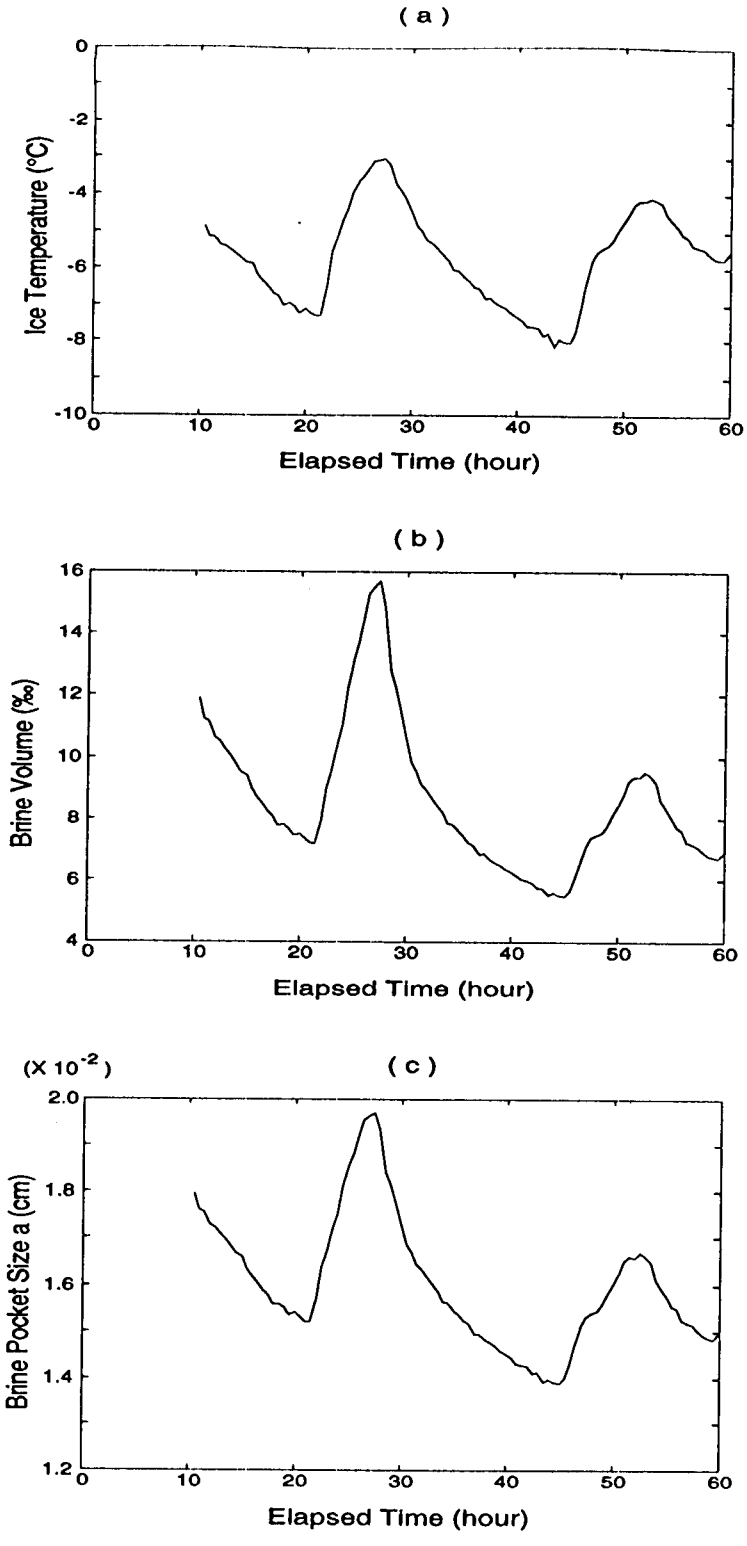

Figure 6: Simulated ice bulk properties as a function of time in the course of ice growth. (a) Ice temperature T_i in $°C$. (b) Brine volume fraction. (c) Bine pocket size a in cm.

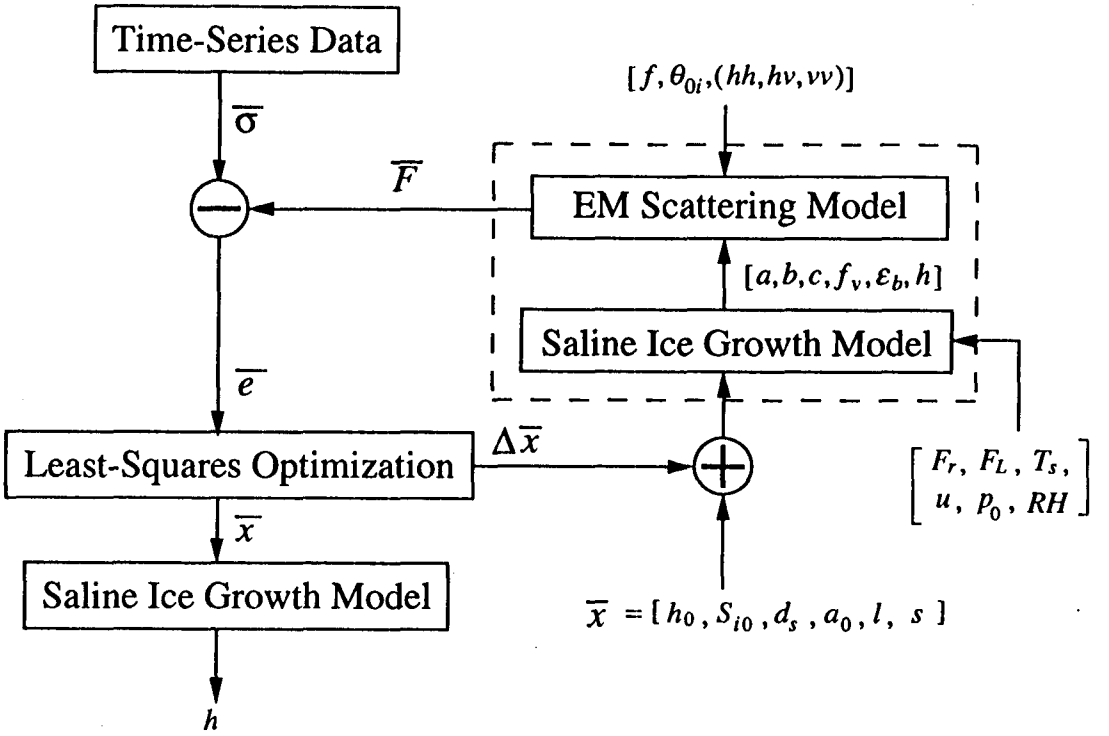

Figure 7: Block diagram of the inversion algorithm using time series measured data. The dynamic electromagnetic scattering model which includes a electromagnetic scattering model and an ice growth model is enclosed by a dashed rectangle.

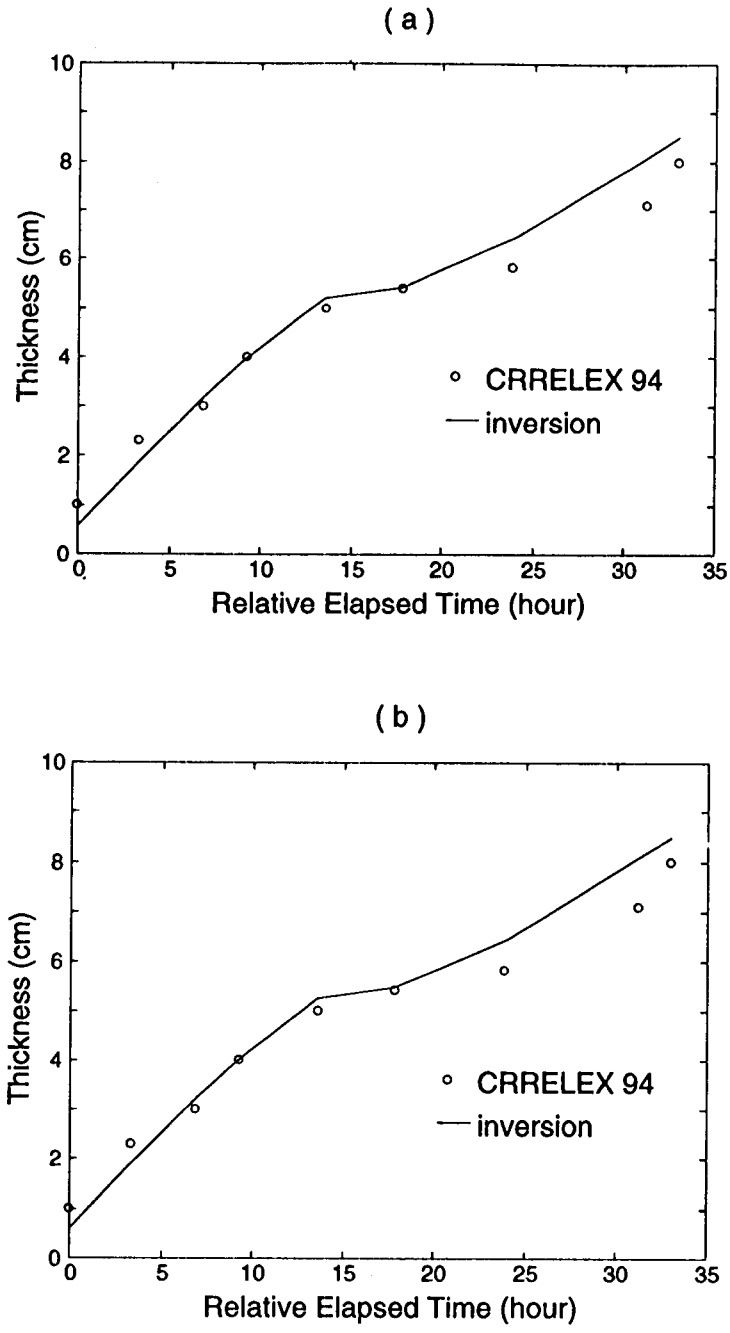

Figure 8: Thickness retrieval using both HH & VV time series data. (a) 30° incidence angle. (b) 40° incidence angle. o represents the measured ice thickness. Solid curve indicates the evolution of reconstructed ice thickness using measured time series data.

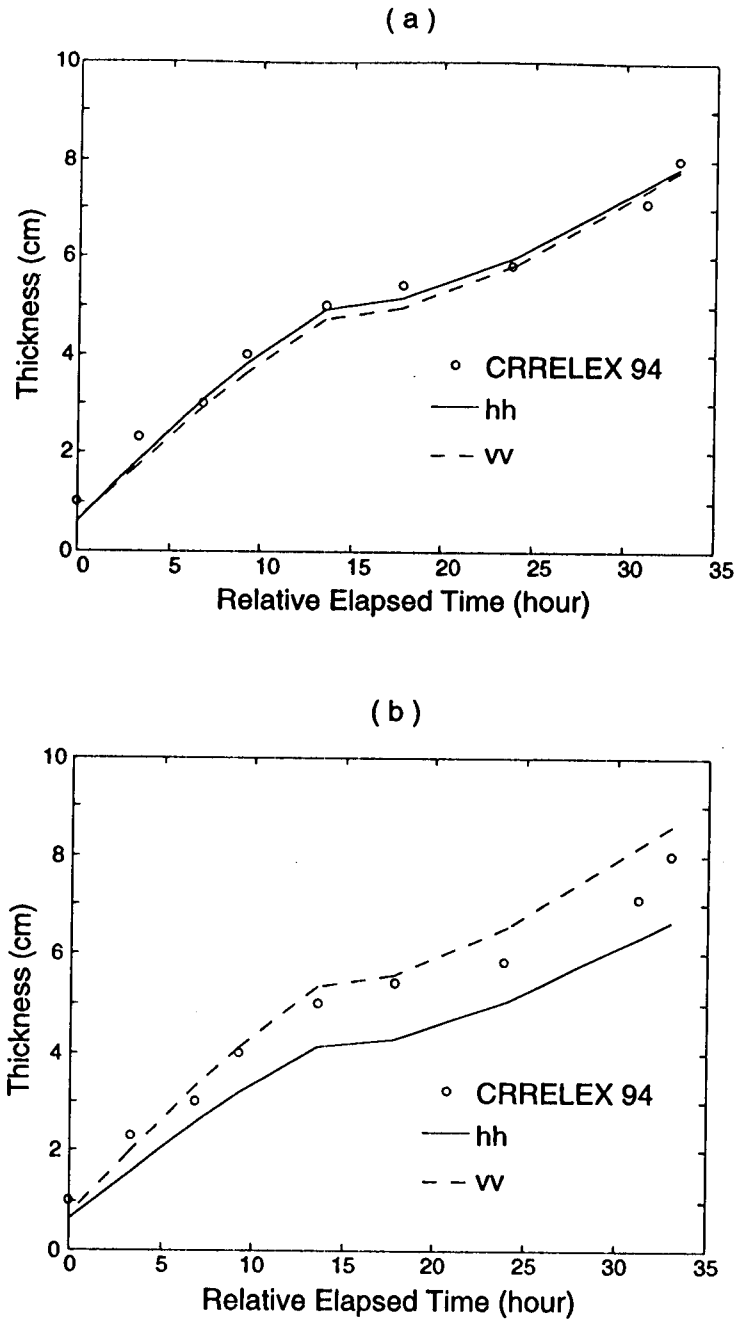

Figure 9: Thickness retrieval using single polarization time series data. (a) 30° incidence angle. (b) 40° incidence angle. o represents the measured ice thickness. Solid curve indicates the evolution of reconstructed ice thickness using measured HH-polarization time series data; dashed curve indicates the evolution of reconstructed ice thickness using measured VV-polarization time series data.

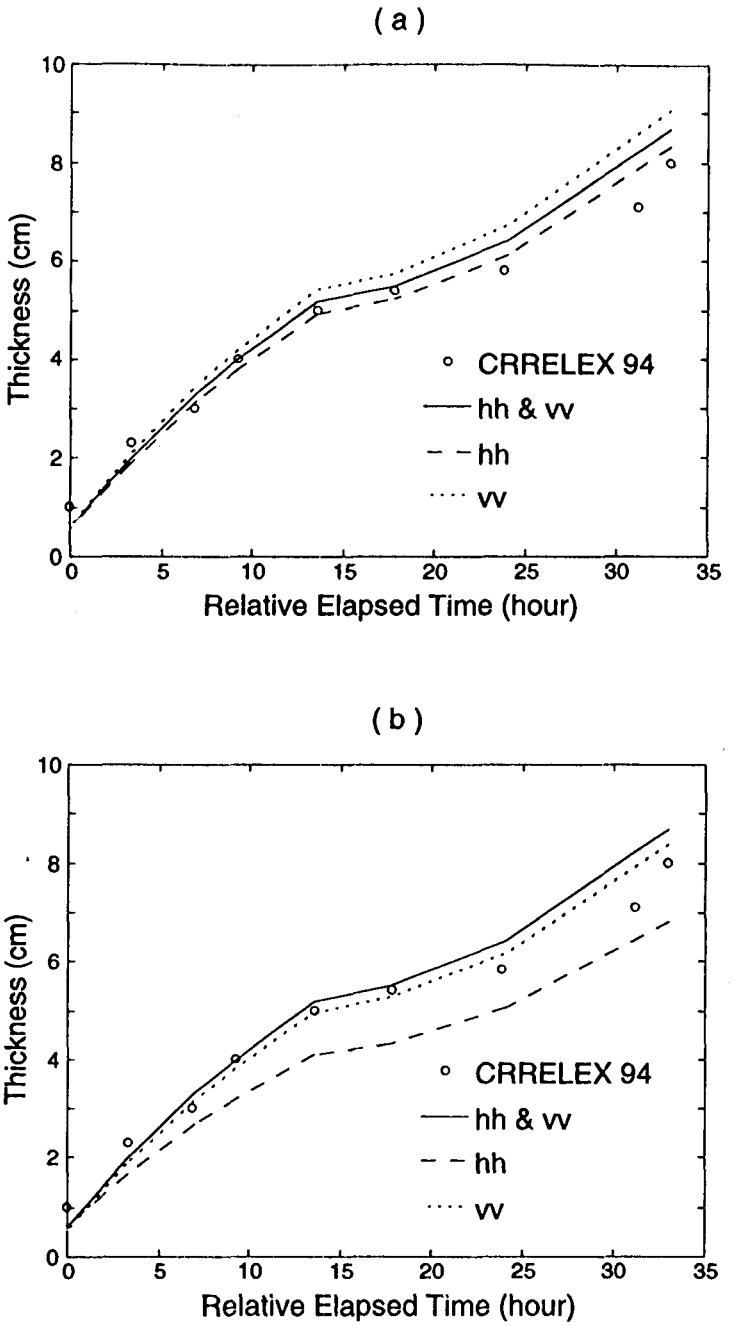

Figure 10: Thickness retrieval using solar radiations and air temperatures. (a) 30° incidence angle. (b) 40° incidence angle. o represents the measured ice thickness. Solid curve indicates the evolution of reconstructed ice thickness using measured both HH & VV time series data; dashed curve indicates the evolution of reconstructed ice thickness using measured HH-polarization time series data; dotted curve indicates the evolution of reconstructed ice thickness using measured VV-polarization time series data.